Design Methodology for Robotic Manipulator for Overground Physical Interaction Tasks

Sambad Regmi
Department of Mechanical and Aerospace Engineering,
Missouri University of Science and Technology,
Rolla, MO 65401
e-mail: srn3p@mst.edu

Yun Seong Song
Department of Mechanical and Aerospace Engineering,
Missouri University of Science and Technology,
Rolla, MO 65401
e-mail: songyun@mst.edu

We present a new design method that is tailored for designing a physical interactive robotic arm for overground physical interaction. Designing such robotic arms present various unique requirements that differ from existing robotic arms, which are used for general manipulation, such as being able to generate required forces at every point inside the workspace and/or having low intrinsic mechanical impedance. Our design method identifies these requirements and categorizes them into kinematic and dynamic characteristics of the robot and then ensures that these unique considerations are satisfied in the early design phase. The robot's capability for use in such tasks is analyzed using mathematical simulations of the designed robot, and discussion of its dynamic characteristics is presented. With our proposed method, the robot arm is ensured to perform various overground interactive tasks with a human. [DOI: 10.1115/1.4045688]

Keywords: physical human–robot interaction, manipulator design, effective impedance, parallel direct drive mechanism, dynamics, haptic devices, mechanism design, parallel platforms, robot design, theoretical kinematics

1 Introduction

Following their success in many industries, robots are now moving to applications that directly affect human movements, such as applications in medicine [1] and healthcare [2,3]. For example, robots have been applied to the rehabilitation and recovery of movement in stroke patients [4–6] or in medical surgery [3,7,8] and have been successful in the past few decades. These more recent applications of robots require them to physically interact with the human body and have further triggered the vision of human-like interactive robots that are capable of safe and effective interaction with humans, even with frail populations.

Imagine a robot helping an elderly person to walk to their day-to-day activities or a robotic partner helping a person prepare to dance: these human replacements could make a large positive impact on an individual's quality of life. Currently available physical interactive robots cannot readily be used in these overground applications, as they are developed to be stationary for seated rehabilitation programs that are intended for the arms only [4–6]. On the other hand, robotic walking partners can prove their usefulness in enhancing gait balance and postural stability, such as in patients suffering from Parkinson's disease [9]. Such overground physical human–robot interaction (pHRI) requires a novel robot with an ability to carry out physical interaction tasks while walking alongside a human.

Despite the potential benefits, it is yet unclear what the expectations and challenges are for a robot to be physically interactive with a human during overground tasks. In order to develop such a robot, one must first understand how humans interact with other humans—epitome for accomplishing physical interaction tasks with or without any verbal and/or gestural information exchange [10,11]. Therefore, if robots are to replicate the interaction characteristics of humans and hence be used in pHRI, a clear prior understanding of humans—complex biological systems, and their ways of communicating motor intent is needed.

What specific human interaction characteristics are we seeking? An interaction is a two-way phenomenon where the information exchange occurs on a give-and-take basis [11]. In many cases, the interaction happens through the arms, through which both power and motor intent are exchanged. Previous physical human–human interaction (pHHI) experiments [12–14] have hinted that arms are used for exchanging motor intent in the form of force and motion during assigned interactive tasks. This view is consistent with an interactive robot controller based on impedance [15] that relates motion to force, rather than considering motion and force independently. Similarly, Ref. [16] has suggested the relationship of low-arm impedance with interaction tasks through small force. Thus, analyzing the real-time impedance of the human arm during small-force physical interaction may be the first critical step to understand the force and motion exchange attributes during physical interactions.

Unfortunately, the existing interactive robots are not suitable for studying human arm impedance during overground interactive tasks. Interactive robot arms such as the Haptic Masters [17], phantom haptic interface [18,19], KIN-ARM [5,20], and MIT Manus [6,21] are fixed to a specific location and are best fitted for traditional seated interaction experiments [4–6,11,13,19,21]. On the other hand, mobile robots [16,22] are not preferable because of their incapability to measure arm impedance of its partner human. Therefore, a new experimental robot is needed that is capable of overground interaction and yet is able to measure arm impedance at the same time. We envision that the robot will consist of a wheeled mobile base and a highly interactive arm (see Fig. 1), where the former part will only be used for locomotion and does not have to consider small interaction forces or impedance measurement; in fact, several available robotic platforms fulfill the overground mobility requirements and hence can be used for the robot's body. On the other hand, the interactive robotic arm is expected to exchange sophisticated interaction with a human partner. Hence, the majority of the design effort should be focused on the interactive robotic manipulator arm.

This paper presents the unique design procedure for the robotic manipulator arm as part of an overground interactive robot. We present the unique and unconventional static and dynamic requirements of the interactive robotic arm in the perspective of measuring human arm impedance during overground interaction tasks, and

Contributed by the Mechanisms and Robotics Committee of ASME for publication in the Journal of Mechanisms and Robotics. Manuscript received August 30, 2019; final manuscript received November 25, 2019; published online December 12, 2019. Assoc. Editor: Damien Chablat.

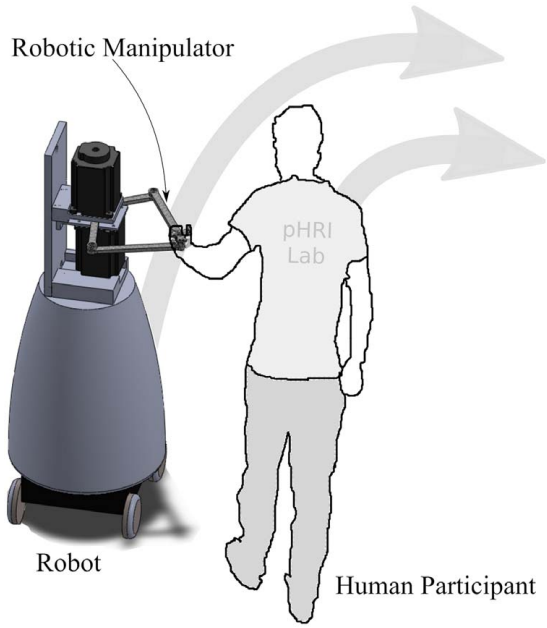

Fig. 1 Envisioned pHRI experiment

thus, present a new design method for physically interactive robotic arm for human arm impedance measurement.

2 Design Requirements

The envisioned overground robot will perform as an interactive system to measure human arm impedance during overground physical interaction. Until now, the design requirements for such robots have not been discussed specifically for overground robots, especially when considering small interaction forces. It is clear that one cannot adopt the same design principles that are used for industrial robots, since the application is vastly different. With our specific goal in mind, we consulted prior literature on stationary interactive robots, light interaction forces, and impedance measurements to devise the unique mechanical design requirements as follows.

2.1 R1: Workspace Requirement. Interaction characteristics information shared in the 2D ground plane may be analyzed with the help of a 2D plane robotic arm aligned in a plane parallel to the ground. As a start, we will consider interaction in a 2D plane, and hence, a 2D plane-parallel robotic arm is chosen over a 3D robotic arm as used in many rehabilitation robots [4–6].

The workspace of our robotic arm was chosen to be 150×150 mm^2. Based on an earlier work on the similar framework (overground pHRI during walking [22]), the distance between the robot and the human partner varied less than 300 mm, where most of the displacement is due to the human arm length change. This suggests that the robot arm is not expected to change lengths as much as the human arm does. Considering a factor of 50%, the robot arm is expected to move less than 150 mm. Hence, our 150×150 mm^2 workspace is expected to be sufficient for our pHRI task, at least as an initial assessment.

2.2 R2: Force Requirement. Our robot must be able to deliver enough force during pHRI. The magnitude of the required force would be comparable to the interaction forces during pHHI, such as in overground walking tasks [14,16] or social handshake [23]. In these work, interaction forces are typically around 10 N with peak forces around 15–25 N. Hence, we set the requirement that our robotic arm must be able to generate interaction forces in the range of 10 N. In other words, the rated force output would be around 10 N with occasional peak force of around 20 N. The robotic manipulator end must satisfy the minimum force requirement at every point inside the workspace, unlike typical manipulator design, which focuses on satisfying the maximum output force only at certain points.

2.3 R3: Endpoint Speed Requirement. The robots involved in the experiment must be able to produce a speed that is similar to the human arm movement during an interaction. Reference [24] has implied that the frequency range of human arm movement is around 2 Hz. Considering a cycle of a corner to corner diagonal movement with the frequency of 2 Hz, the speed requirement inside the workspace is 0.8485 m/s.

2.4 R4: Impedance Requirement. The planar robotic arm must have a low intrinsic mechanical impedance in order to be interactive (back- drivability). This also helps with the human arm impedance measurement, because with low impedance, the robot arm will feel smoother and less cumbersome, and consequently, the human partner will more naturally interact with the robot without artificially stiffening his/her arm. While the apparent mechanical impedance of a robotic manipulator can be reduced by feedback control, it is nonetheless preferable to have low passive impedance to begin with, such as having low inertia or damping.

3 Kinematic Considerations

3.1 Linkage Design. Manipulators, based on the serial drive mechanism, are more popular than their closed-loop chain counterparts because parallel mechanisms are less intuitive to implement due to their complex geometry, nonlinear dynamics, and workspace constraints. However, when considering factors such as high speed, high accuracy, high precision, high acceleration, high stiffness, high load carrying capacity, and/or low inertia, these parallel manipulators may be advantageous over manipulators that are based on the serial drive mechanism [25]. One can find useful examples in various applications: industrial applications such as Hexapods or Delta Robots, medical applications such as the Stewart Platform for precision surgery, and space application such as satellite trackers for better orientation are just a few examples for these types of manipulators [26]. For our application, a platform manipulator [25]—Closed-loop five links mechanism (CLFLM)—is selected, so that, in addition to satisfying planar design requirement in R1, it will also extricate robotic links from carrying heavy motors.

We note that the workspace of the closed-loop robotic linkage is smaller than that of similar sized serial robot manipulators [25,27,28]. This is due to the singularities in the closed-loop linkage mechanism that restricts the smooth and continuous use of the reachable workspace. Despite this workspace restriction, due to the aforementioned advantages and in order to measure small impedances precisely and accurately, parallel manipulators are preferable [25].

First and foremost, the CLFLM has to satisfy the workspace area requirement in R1 that governs the design's final length of the links. Furthermore, the length of the links has to be tailored to their optimal value in order to minimize the inertia. Figure 2 shows a schematic representation of the robotic arm (M_1ACBM_2) with its end effector (C) inside the workspace ($T_1T_2T_3T_4$). Let one motor (M_1) be lodged at the origin represented in the global coordinate system and another motor (M_2) at any other point (X_0, Y_0) in the 2D space. Table 1 includes the symbols for various parameters that are used for the robotic manipulator.

Based on the preliminary knowledge of CLFLM and their previous use in human–robot interaction experiments, the following considerations are made regarding the length of the links:

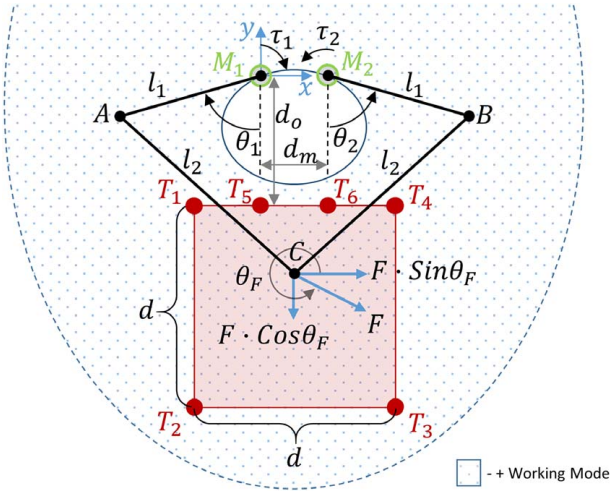

Fig. 2 Sketch of the robot arm and its workspace

Table 1 Nomenclature of parameters used in the robotic manipulator

Symbols	Parameters
l_i	Length of the link ($i = 1, 2$)
τ_j	Torque applied by the motor ($j = 1, 2$)
θ_k	Angle made by the link ($k = 1, 2$)
d_0	Distance from the origin to the top of the workspace
d	Length and width of the workspace
F	Force applied on the end effector
θ_F	Angle at which force (F) is applied
d_m	Offset distance between the motors

Note: All angles are measured in CCW direction with respect to the positive x-axis. Torque convention is positive in CCW direction

3.1.1 A1: Symmetricity of the Mechanism. The robotic arm should be unbiased with respect to the motor locations. This means that the human must not receive any clues of the end effector's location due to the asymmetry of the design itself. Even parallel manipulators used in industries for pick and place operations generally make use of the direct drive mechanism to justify their two degrees of freedom (DOF) requirement, and they are symmetric as well [29]. In this view, a parallel direct drive mechanism based robotic manipulator that is symmetric with respect to its mid-axis between the motors is desired.

3.1.2 A2: Avoid Singularities

- A2 (a): The workspace defined by forward kinematics does not differentiate various segments of the workspace that are divided by singularities. In Refs. [28,30,31], the authors have distinguished three different types of singularities—type 1, type 2, and type 3, and Ref. [27] has classified the workspace into four different segments inside which the mechanism does not suffer any singularity. Out of four segments in Ref. [27], only the working modes "+ −" or "− +" can be used if A1 has to be satisfied. However, larger dexterous workspace can be exploited using mode "− +" than by using "+ −". Hence, choosing the convex pentagon structure (the working mode "− +") yields the largest workspace segment (dotted space in Fig. 2) while satisfying A1, and avoiding singularities as well.
- A2 (b): Restricting the internal angle between the crank link and coupler link to be greater than 15 deg and less than 165 deg avoids type 1 singularity, whereas imposing the same condition for the angle between coupler links avoids type 2 singularity.

3.1.3 A3: Other Kinematic Considerations

- A3 (a): Keeping all other parameters constant, the workspace area is inversely proportional to the offset distance between the motors (d_m) (ground link M_1M_2 in Fig. 2) [27]. It is thus preferable to have small d_m.
- A3 (b): Ref. [32] discussed the advantages of using small crank (proximal link, l_1) in five bar linkages. On the other hand, the small crank to ground link ratio (l_1/d_m) is desirable for favorable mechanical advantage and minimizing inertia [33]. However, A3 (a) discourages the use of the ground link with higher length. Hence, a trade-off between the length of the crank (l_1) and the length of the ground link (d_m) has to be made.
- A3 (c): an arbitrary safe distance (d_0) from the motor to the workspace must be assumed.

In addition to A3 (b), which requires the length of the crank (l_1) to be minimum, minimizing the length of the distal links (l_2) is also crucial in order to decrease the overall inertial of the robotic arm. The method of inequality is deployed to estimate the minimum length of the links. To begin with, the initial approximation of the length of the links is taken from Ref. [34]. The approximated length of the links, which is 25 mm for proximal links and 45 mm for distal links, are linearly magnified by four times to align with R1. Using the forward kinematics of the robotic manipulator, an iterative process is followed on those magnified lengths, which is 100 mm for proximal links, and 160 mm and 180 mm for distal links, so as to approximate the appropriate location of the workspace on the 2D plane. The iterative approximation process suggested that the safe working distance (d_0) can be 95 mm (A3(c)). Given A1, we picked equal proximal links and equal distal links. Considering A3(a) and A3(b) during the iterative process helped us approximate the length of the ground link for our robotic arm (d_m) to be 40 mm.

Given that we have the length of the ground link and the safe workspace distance, we can properly specify motor positions and the location of the workspace in a 2D space. The relationship between the length of the links and the location of the workspace can now be represented in terms of inequality.

$$l_1 + l_2 > M_1T_i \tag{1}$$

$$l_1 - l_2 < M_1T_i \tag{2}$$

$$l_1 > 0 \quad \text{and} \quad l_2 > 0 \tag{3}$$

To align with the angle constraint on A2 (b), further inequality has to be added:

$$\frac{\pi}{180}15 \text{ deg} < \cos^{-1}\left(\frac{l_1^2 + l_2^2 - M_1T_i^2}{2\, l_1\, l_2}\right) < \frac{\pi}{180}165 \text{ deg} \tag{4}$$

where M_1T_i is the shortest distance between motor one (i.e., origin) and the different points selected on the boundary of the workspace, where $i = 1, 2, 3, 4, 5, 6$. The former four points represent the four corners of the workspace, and the latter two are chosen such that they fall on the upper boundary of the workspace right below the motors. It is to be noticed that the farthest and the nearest point of the workspace from the origin (i.e., M_1) are, respectively, T_3 and T_5, and so are T_2 and T_6, respectively, from M_2.

Equations (1)–(4) give a total of 26 inequalities—six from Eq. (1), six from Eq. (2), two from Eq. (3), and 12 from Eq. (4)—that have to be plotted, and the common region that satisfies all of them has to be identified. Solving the inequality constraints results in the common region with different pairs of the length of links (l_1, l_2). However, if any pair (l_1, l_2) satisfies Eq. (4), it eventually satisfies Eqs. (1) and (2); plotting only the

latter two inequalities (Eqs. (3) and (4)) will give a set of solutions. The solution that we want among the set of feasible solutions—(l_1, l_2)—is one that satisfies small crank requirement (A3(b)) as well.

The common solution (see Fig. 3) is governed only by the following four inequalities (out of 26), and the solution obtained also satisfies all the other 22 inequalities discussed earlier.

$$\frac{\pi}{180}15 \text{ deg} < \cos^{-1}\left(\frac{l_1^2 + l_2^2 - M_1 T_5^2}{2\, l_1\, l_2}\right) \tag{5}$$

$$\cos^{-1}\left(\frac{l_1^2 + l_2^2 - M_1 T_3^2}{2\, l_1\, l_2}\right) < \frac{\pi}{180}165 \text{ deg} \tag{6}$$

$$l_1 > 0 \quad \text{and} \quad l_2 > 0$$

The shaded region ABC in Fig. 3 is the common solution, and any pair (l_1, l_2) that falls inside the region meets R1, A1, A2(a), A2(b), A3(a), and A3(c). Considering A3(b), the length of the links (87.74, 177.51) (mm) has to be selected. However, we wanted to have a safe margin to type 1 singularity, even safer than the constraint proposed in A2 (b), that lead us to choose the length of links to be (110, 175) (mm). The finalized length of the links—proximal links (l_1) = 110 mm and distal links (l_2) = 175 mm—are in a comparable range to that of the approximated length of the links after magnification, as mentioned earlier.

It is to be noted that the idea to deploy an iterative process to find the workspace location (d_m and d_0) and then the method of inequality to find the length of the links may not be the only possible and effective way to do so. However, this seems to be a simpler way to obtain the approximate minimum length of the links and the workspace location. Moreover, regardless of how those parameters are obtained, it is to be understood that the overall mechanism has to qualify all the dynamic considerations (as in Sec. 4) and hence satisfy the impedance requirement (R4). In this view, starting with a simple and intuitive iterative process and using inequalities may be sufficient for our work—especially when the identified length of the links satisfies dynamic considerations as will be shown in Sec. 4.

In a pursuit to find the approximate minimum length of links and the workspace location with teachings from prior art, the loop closure equation method [35] was also investigated. This numerical iteration technique makes use of equations based on the trigonometric relationship of the mechanism on different configurations. In order to get a unique solution, the number of equations used must be equal to the number of unknowns to be solved. If this is not the case, the difference between available equations and unknowns can be chosen as free choices, as per our design requirements.

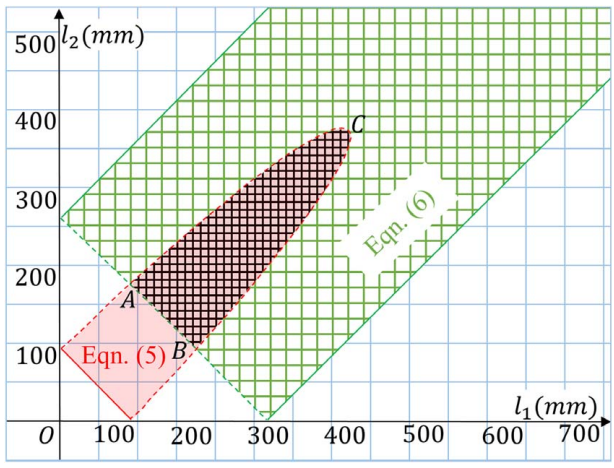

Fig. 3 The inequalities plotted in the $l_1 - l_2$ space

However, those free choices have to be chosen carefully so that there should be a viable mechanism available with the choices. In our context, we had too many unknowns to be solved using a few equations leading toward many free choices that had to be assumed. In the aforementioned work that uses the method of inequality, an iterative process had to be deployed even before deploying the method to approximate d_m and d_0. If these two constants in the method of inequality are compared with the free choices in the loop closure equation method, then it should be well understood that the process of picking the free choices itself is going to be computationally difficult and time consuming, even before starting to solve the equations using the loop closure equation method. In addition, being a numerical iteration technique, the variables whose values are sought have to be assumed beforehand and should be in close proximity to the values of the original solution.

With 10 equations and 14 unknowns to solve for our direct drive CLFLM, we were left to pick four free choices and 10 initial guesses. It is very difficult to choose four free choices that comprise a real mechanism as well as 10 initial guesses that need to be in a close proximity range to their respective real solution. To some extent, this hassle can be minimized by constraining the CLFLM to one DOF system—such as in Ref. [35]. However, constraining DOF is not feasible in direct drive mechanisms. Hence, the idea to use the loop closure equation method seems tedious and overly complicates the design process for our direct drive CLFLM robotic arm.

3.2 Motor Selection. For the end effector to satisfy R2 and R3, the selection of a right motor—based on torque and angular speed—is crucial. This implies that a proper relationship between the linear speed and force requirement of the end effector needs to be converted to the minimum torque and angular speed requirement of the motors, respectively. Moreover, these requirements must be satisfied for each and every configuration defined inside the workspace; unlike industrial robot design, where a specific force is required at a small number of endpoint positions, our robotic arm must satisfy the force and velocity requirements within the whole workspace. This is because human–robot interaction can occur at any given configuration of the robot.

We begin with the kinematic equations:

$$\tau = J^T F \tag{7}$$

$$\omega = J^{-1} V \tag{8}$$

where, $[\tau_1(\theta_1, \theta_2, F, \theta_F)\ \tau_2(\theta_1, \theta_2, F, \theta_F)]^T \triangleq \tau$, $J(\theta_1, \theta_2) \triangleq J$, $[\omega_1(\theta_1, \theta_2, V, \theta_F)\ \omega_2(\theta_1, \theta_2, V, \theta_F)]^T \triangleq \omega$, F, and V are torque vector, Jacobian matrix, angular speed vector, external force vector, and linear velocity vector at the effector, respectively.

In order to solve for τ (motor torque required to produce an output force F) and ω (motor angular velocity required to produce end-effector velocity of V) within the entire workspace, it is unrealistic to attempt to find closed-form solutions due to the presence of motor angle (θ_1, θ_2)-dependent Jacobian matrix. Instead, a close-enough solution is sought by sampling a finite number of endpoint positions and solving Eqs. (7) and (8) at these specific points. This notion of selecting a finite number of endpoint positions to from a sampling region is similar to the work with feasible point-to-point trajectories in Ref. [30].

About 130 × 130 uniformly distributed sample points were chosen from the workspace such that each point represents the combinations of angular displacement of motors (motor M_1 and motor M_2) in 1 deg increments within their operational range. Considering the length of the links and other parameters (d, d_0, and d_m) obtained in Sec. 3.1, we determined that the operational range for θ_1 and θ_2 is between 135.6 deg (end-effector at points T_2 and T_3) and 7.6 deg (end-effector at points T_5 and T_6). Then, if S_1 and S_2 are sets of angles of θ_1 and θ_2, respectively, each sample point can be identified

as the combination of elements from these two sets.

$$S_1 = \{136 \text{ deg}, 135 \text{ deg}, \ldots, 6 \text{ deg}\} \quad (9)$$

$$S_2 = \{136 \text{ deg}, 135 \text{ deg}, \ldots, 6 \text{ deg}\} \quad (10)$$

In addition, at any specified point inside the workspace (for example, $\theta_1 = 100$ deg and $\theta_2 = 100$ deg), the torque requirement of the motor is dependent on the magnitude as well as the direction of F and so is for the angular speed requirement of motor, which is dependent on the magnitude as well as the direction of V. This direction dependency of torque and angular speed necessitates the introduction of the third set (S_3) that addresses the direction of application of specified magnitude of force or velocity at the end effector.

$$S_3 = \{0 \text{ deg}, 1 \text{ deg}, \ldots, 359 \text{ deg}\} \quad (11)$$

A configuration set S of triples taking each element from S_1, S_2, and S_3 is constructed and is shown in Eq. (12). The motor torque (τ) and the angular speed (ω) will depend on which element in set S we are considering with a total of $131 \times 131 \times 359 = 6,160,799$ scenarios.

$$S = \left\{ \begin{matrix} (136 \text{ deg}, 136 \text{ deg}, 0 \text{ deg}), (136 \text{ deg}, 136 \text{ deg}, 1 \text{ deg}), \\ (136 \text{ deg}, 136 \text{ deg}, 2 \text{ deg}), \ldots, (136 \text{ deg}, 135 \text{ deg}, 0 \text{ deg}), \\ \ldots, (6 \text{ deg}, 6 \text{ deg}, 359 \text{ deg}) \end{matrix} \right\} \quad (12)$$

3.2.1 Force Requirement. To find the motor torques, given the estimated typical magnitude of F of 10 N (as in R2), using Eq. (7) (kinematic equation), an online solver is designed that updates the required parameters in Eq. (7) and calculates the torque requirement of the motor for each and every triple in the set S. The output of the solver is a torque matrix T such that the first row constitutes all possible τ_1 values and the second row constitutes all possible τ_2 values (see Fig. 2) calculated for each element of the set S.

$$\mathrm{T} = \begin{bmatrix} \tau_{11} & \tau_{12} & \tau_{13} & \cdots & \tau_{1k} \\ \tau_{21} & \tau_{22} & \tau_{23} & \cdots & \tau_{2k} \end{bmatrix}$$

where $k = 6,160,799$. Each column of the matrix can be visualized as the torque vector τ that is required to resist/produce F force applied at a specific angle θ_F at the end effector for a specific configuration (θ_1, θ_2) of the robotic arm. The element-wise max norm of the matrix T ($\|T\|_{\max}$) gives the torque required for motors that satisfy minimum force requirement (R2) at each and every point inside the workspace.

3.2.2 Velocity Requirement. Similar to the torque solver, given the maximum magnitude of V of 0.8485 m/s (as in R3), a separate solver is designed that updates the required parameters in Eq. (8) and calculates the angular speed requirement of the motor for each and every triple in set S. The output of the solver is a speed matrix W such that the first row constitutes all possible ω_1 values, whereas the second row constitutes all possible ω_2 values for each element of set S.

$$W = \begin{bmatrix} \omega_{11} & \omega_{12} & \omega_{13} & \cdots & \omega_{1k} \\ \omega_{21} & \omega_{22} & \omega_{23} & \cdots & \omega_{2k} \end{bmatrix}$$

Each column of the matrix W can be visualized as the speed vector ω that is required to produce V velocity at the specific angle θ_F at the end effector for a specific configuration (θ_1, θ_2) of the robotic arm. The element-wise max norm of the matrix W ($\|W\|_{\max}$) gives the angular speed required for motors that satisfy the endpoint speed requirement (R3) at each and every point inside the workspace.

The motors' minimum output torque requirement and minimum angular speed requirement based on the force requirement (R2) and the linear speed requirement (R3) were found to be 1.2581 Nm and 401.5697 rpm, respectively. The motor BLY343D-48V-3200-7200SI (Anaheim Automation, Inc.), which has a rated output of 1.4 Nm and a rated speed of 2700 rpm, is chosen.

4 Dynamics Characteristics

In this section, a mathematical simulation model that resembles the real physical system is developed using the dynamics of the robotic arm in order to observe the mechanical impedance characteristics and thereby scrutinize the robotic manipulator's efficacy in precise and accurate impedance measurement tasks (R4).

Inertial and frictional losses are inevitable in any robotic system. However, when we discuss about very low interaction forces and impedances, reducing these losses as low as possible is strongly preferable. While one can reduce the apparent inertia and damping through feedback control, it is nonetheless preferred to have a low intrinsic (passive) inertia and damping to begin with.

To examine the passive mechanical impedance of our robot arm, we want to analyze the effective inertia (EI) and the effective damping coefficient (ED). The dynamics of a robot is defined by its equations of motion. Since most robotic arms do have complex dynamics, it is often not a necessity to derive such equations unless a robotic simulator model of the manipulator is desired. In some circumstances, such as this work where a robotic simulator is required beforehand to examine its inertia and damping behavior, or sometimes for designing the nonlinear control strategies (such as backstepping controllers and sliding mode controllers), equations of motion are necessary to be derived.

It is a common practice to apply the Euler Lagrangian method to develop the equations of motion of the complex system by using energy equations. All the parameters associated with the robotic arm (such as masses of individual links, frictional damping coefficient, and rotor inertia of the motors) have to be defined beforehand. These parameters for our robotic arm are given in Table 2. The developed coupled second-order equation resembles the standard robotic manipulator equation as given in Eq. (13).

$$M(\theta)\ddot{\theta} + V_m(\theta, \dot{\theta})\dot{\theta} + \tau_r(\dot{\theta}) + G(\theta) + \tau_d = \tau + J^T(\theta)\lambda \quad (13)$$

where $\theta(t) \in [\theta_1 \ \theta_2]^T$ is the joint space coordinate vector, $\tau(t) \in [\tau_1 \ \tau_2]^T$ is the control input vector, $M(\theta(t))$ is the inertia matrix, $V_m(\theta(t), \dot{\theta}(t))$ is the Coriolis/Centripetal matrix, $\tau_r((t))$ are the friction terms, $G(\theta(t))$ is the gravity vector, and τ_d represents disturbances. $J(\theta)$ is the Jacobian matrix associated with the contact surface geometry, and λ (the so-called "Lagrange multiplier") is a vector of contact forces exerted on the external environment.

Considering an ideal condition, any disturbances ($\tau_d = 0$) will not be taken into account. Likewise, the effect of gravity is also ignored, considering its planer 2D geometry that will be placed parallel to the ground $G(\theta(t)) = 0$.

$$M(\theta)\ddot{\theta} + V_m(\theta, \dot{\theta})\dot{\theta} + \tau_r(\dot{\theta}) = \tau + J^T(\theta)\lambda \quad (14)$$

All the matrices, M, V_m, and J, and the vector τ_r, do have complex nonlinear terms in them and require the parameters from Table 2 to

Table 2 Values for parameters used in the robotic simulator

Parameter	Value
Mass of each proximal link of the manipulator	0.11 kg
Mass of each distal link of the manipulator	0.175 kg
Rotor inertia of each motor	0.00016 kg m^2
Width of individual link	0.015 m
Inner diameter of the bearings	0.008 m
Outer diameter of the bearings	0.014 m
Frictional damping coefficient (b) of the bearings	0.0169 kg m^2/s

Note: SMR148 bearings (Boca Bearing Company) are used in robotic joints. The frictional damping coefficient (b) of the individual bearing is approximated based on frictional power loss versus rolling speed relationship plots in Ref. [36].

be substituted in addition to the values of parameters defined in Table 1, which are mostly configuration dependent. All these parameters are already obtained in the previous sections of this paper.

An exception to all known parameters is the frictional damping coefficient for the bearing used, which we estimated using prior work. The friction on a mating surface (ball and bearing's surfaces) in a ball bearing is a function of surface and load applied only and does not depend upon the system's dynamic characteristics. The friction in the bearing surface, however, is a function of angular velocity as well [36,37]. Due to the lack of literature on computing friction of deep groove ball bearing, we used the relation established by Ref. [36] on the deep groove ball bearing SKF-6205, which has an inner diameter (ID), outer diameter (OD), and width (h) of 25 mm, 52 mm, and 15 mm, respectively. By assuming the maximum rolling speed for our bearing SMR148, the respective maximum bearing friction power loss under zero circumference radial preload and no lubrication was obtained. Since the dimension of SKF-6205 bearing does not match with the dimension of our bearing, which has ID, OD, and h of 8 mm, 14 mm, and 3.5 mm, respectively, we linearly reduce the result obtained by 16 times. Now the linear relationship between the angular speed and the power loss was exploited to calculate the maximum damping coefficient of the system and is given in Table 2.

The model (as shown in Eq. (14)) can now be used to study EI and ED of the physical robotic systems. However, since EI and ED depend not only on the configuration (such as S defined in Sec. 3.2) but also on velocities and accelerations, it is unrealistic to attempt to calculate EI and ED for every possible scenario. Instead, we considered a number of hypothetical, representative interaction tasks and found EI and ED at the initiation of these tasks only. In these tasks, we assume that a human applies a force at a number of initial configurations (details presented hereafter in this section). This can be interpreted as the opposing force the human subject feels when an interaction is initiated on a passive robot arm.

Considering no externally applied torque at the actuators ($\tau = 0$ in Eq. (14)), we will analyze only the y-component of both EI and ED when a constant force $F = 10$ N is applied on the end effector through the center of the workspace ($\theta_1 = \theta_2$) at an angle of 270 deg CCW with respect to positive x-axis as shown in Fig. 4(*a*). In this scenario, due to the symmetricity of the system (A1) and force being applied through its mid-axis, the change in position of the links at any instant becomes symmetric, and so is the angle pair (θ_1, θ_2), where $\theta_1 = \theta_2 = 34.29$ deg, …, 102.97 deg, (notated as (θ_s, θ_s) here onward for any configurational geometry in the end effector's path. Even though it does not remove the nonlinearity in the system, it will comparatively simplify the task to analyze EI and ED; it is easier to relate the inertial and damping behavior when they are applied in a specific direction and through a symmetric pathway.

The experimental case designed here is solely a representative experiment, and hence, we do not expect them to fetch generalized EI and ED values for entire arm configurations. Nonetheless, the respective representative values help us find out the overall effectiveness of the robotic arm. Furthermore, this analysis scenario is likely to happen in the actual pHRI experiment as well; during pHRI experiment, we intend to study the process of information exchange in a direction aligned parallel to the symmetric mid-axis of the robotic arm. The techniques to obtain EI and ED values for more complex scenarios are discussed in Sec. 4.1.

Our procedure for estimating EI and ED for an ideal experimental case designed earlier is as follows. For every (θ_s, θ_s), we assume zero initial velocity, apply force F at the end effector, simulate the resulting position, velocity, and acceleration during a short time interval, $t = [0, 0.05]$ s, and then calculate EI and ED based on the linear force-velocity-acceleration relationship observed at this time interval.

In order to estimate EI, we first assume an undamped system where the passive impedance is solely due to the inertia. Using an ideal undamped robotic arm similar to Eq. (15), we select (θ_s, θ_s) configuration and apply the aforementioned interaction scenario. The EI for the specific configuration was estimated by using linear force-acceleration relationship as given in Eq. (16). Repeating the procedure for all individual starting configurations (θ_s = 103 deg, 102 deg, 101 deg, …, 34 deg), we found EI as shown in Fig. 4(*b*).

Next, ED is further estimated as follows. A similar procedure was carried out with a damped simulator system (Eq. (14)). A separate

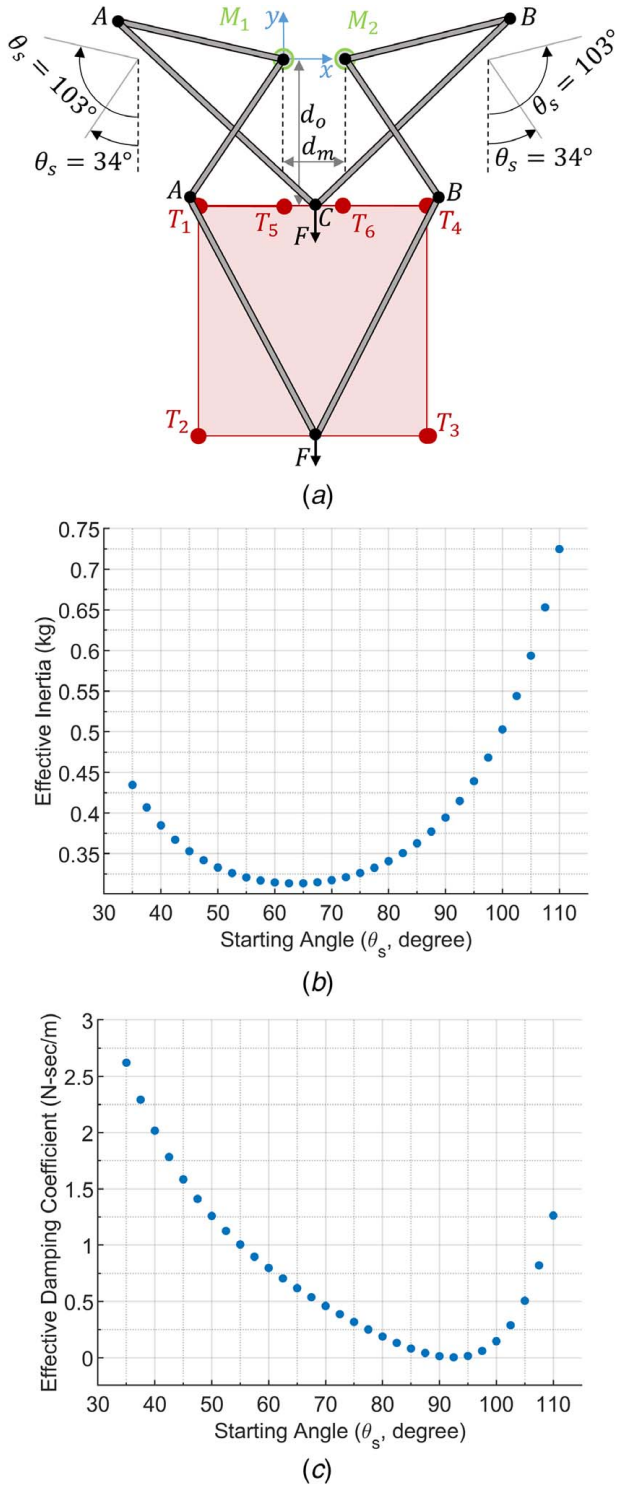

Fig. 4 Mathematical simulation setup and results: (*a*) robotic manipulator at angles $\theta_s = 103$ deg and $\theta_s = 34$ deg, (*b*) effective inertia (EI) versus starting angle (θ_s), and (c) effective damping coefficient (ED) versus starting angle (θ_s)

set of velocity and acceleration data were calculated. We used configuration-dependent EI values found previously along with the new velocity and acceleration data to calculate the purely velocity-dependent interaction, from which ED can be estimated using Eq. (17).

$$M(\theta)\,\ddot{\theta} + V_m(\theta,\ \dot{\theta})\,\dot{\theta} = J^T(\theta)\lambda \tag{15}$$

$$EI = \frac{F}{a_u} \tag{16}$$

$$ED = \frac{F - EI\ a_d}{v_d} \tag{17}$$

where a_u, a_d, and v_d are accelerations of the undamped system, acceleration of the damped system, and velocity of the damped system, respectively, each measured at 0.05 s after the force had been applied on the $(\theta_s,\ \theta_s)$ configuration. It is to be noted that the effective damping force for any specific configuration can be calculated by using Eq. (18).

$$\text{Damping force} = ED\ v_d \tag{18}$$

The cumulative mass of the robotic manipulator links at rest is 0.57 kg. In Fig. 4(*b*), the range of EI is found to be within an average value of 0.396922 kg with the maximum value being 0.7247 kg. The maximum ED during initiation of interaction is found to be 2.6 N s/m at 34 deg starting angle. Taking the maximum velocity to be 0.8485 m/s (R3), the maximum effective damping force that the user will feel during an interaction is estimated to be 2.2061 N. The result shows that the robotic arm will not be too bulky while initiating the interaction and is acceptable for pHRI experiments.

4.1 Interpretation of the Simulation Results. Some values for ED in Fig. 4(*c*) are very low, even as low as zero. This suggests that the damping force felt on those specific configurations may be negligible. This may be explained by the fact that some earlier literature have pointed out the existence of negative damping at low velocities [37,38]. Our approach in estimating EI and ED may not be the most reliable for continuous motion of the end effector. Nonetheless, our approach provides us with reasonable expected values of EI and ED near the center of the workspace which is where most interactions will occur. We used the simulated dynamics to estimate the EI and ED at the initiation of an interaction task and not during the time course of the interaction task. This was deliberately planned to avoid nonlinear effects that may complicate the analysis. For example, different EI and ED values may be obtained from the same endpoint position if the accelerations and velocities are different, complicating the interpretation of the result. In fact, our prior, prolonged and extensive attempts on obtaining EI and ED over a continuous longer period of time and displacement was unsuccessful, possibly due to the high complexity of the dynamics.

Earlier in this section, we used a technique to calculate EI, and ED values for ideal representative case designed to simplify the analysis. The technique can also be extended to any general scenarios in order to compute EI and ED values for complex unsymmetrical configurations. Given a point on the workspace, one can apply forces in two or more directions and find the two-by-two EI and ED matrices as follows:

Equations (16) and (17) have to be modified accordingly to Eqs. (19) and (20), respectively.

$$\begin{bmatrix} F_x \\ F_y \end{bmatrix} = \begin{bmatrix} EI_{xx} & EI_{xy} \\ EI_{yx} & EI_{yy} \end{bmatrix} \begin{bmatrix} a_{ux} \\ a_{uy} \end{bmatrix} \tag{19}$$

$$\begin{bmatrix} F_x \\ F_y \end{bmatrix} = \begin{bmatrix} EI_{xx} & EI_{xy} \\ EI_{yx} & EI_{yy} \end{bmatrix} \begin{bmatrix} a_{dx} \\ a_{dy} \end{bmatrix} + \begin{bmatrix} ED_{xx} & ED_{xy} \\ ED_{yx} & ED_{yy} \end{bmatrix} \begin{bmatrix} v_{dx} \\ v_{dy} \end{bmatrix} \tag{20}$$

where a_{u-}, a_{d-}, and v_{d-} are accelerations of the undamped system, acceleration of the damped system, and velocity of the damped system, respectively in x- or y-direction, each measured at 0.05 s after the force had been applied at the endpoint at the configuration of interest. F_x and F_y are the components of force applied in x- and y-directions, respectively. With two force directions and two resulting acceleration vectors, one can solve for the four elements of EI matrix in Eq. (19). Then, with two more application of forces and their resulting acceleration and velocity vectors, one can solve for the four elements of ED matrix in Eq. (20). One may also choose to apply more than two directions of forces to either or both Eqs. (19), and (20) and apply linear least squares regression to find the elements of EI and ED matrices [39].

5 Future Works

Our next step is to build a real physical system based on the design requirements set in this paper. Furthermore, we will continue our work to develop the control strategies required for physical interaction with a human. After the robotic arm is built, we will apply our methods discussed in Sec. 4 with the built robotic arm as well. It is also of utmost importance to find a proper mobile robotic platform base on top of which the developed robotic arm will be lodged. The base also has to ensure that the function of the robotic arm will not be affected during the overground movement. During the assembly of the arm and the base, proper coordination between them has to be ensured as well. The robotic arm in combination with a mobile robotic platform will be used in our future overground pHRI experiments and expected to be an efficient tool to sufficiently capture human interaction characteristics.

References

[1] Preising, B., Hsia, T. C., and Mittelstadt, B., 1991, "A Literature Review: Robots in Medicine," IEEE Eng. Med. Biol. Mag., **10**(2), pp. 13–22.

[2] Broadbent, E., Stafford, R., and Macdonald, B., 2009, "Acceptance of Healthcare Robots for the Older Population: Review and Future Directions," Int. J. Soc. Rob., **1**(4), pp. 319–330.

[3] Kim, J., Gu, G. M., and Heo, P., 2016, *Biomedical Engineering: Frontier Research and Converging Technologies*, H. Jo, H. Jun, J. Shin, and S. Lee, eds., Vol. 9, Springer, Cham, pp. 489–501.

[4] Chang, W. H., and Kim, Y.-H., 2013, "Robot-Assisted Therapy in Stroke Rehabilitation," J. Stroke, **15**(3), pp. 174–181.

[5] Dukelow, S. P., Herter, T. M., Moore, K. D., Demers, J., Glasgow, J. I., Bagg, S. D., Norman, K. E., and Scott, S. H., 2010, "Quantitative Assessment of Limb Position Sense Following Stroke," Neurorehabil. Neural Repair, **24**(2), pp. 178–187.

[6] Krebs, H. I., Palazzolo, J. J., Dipietro, L., Ferraro, M., Krol, J., Rannekleiv, K., Volpe, B. T., and Hogan, N., 2003, "Rehabilitation Robotics: Performance-Based Progressive Robot-Assisted Therapy," Auton. Robots, **15**(1), pp. 7–20.

[7] Nishihara, S., Sugano, N., Nishii, T., Tanaka, H., Nakamura, N., Yoshikawa, H., and Ochi, T., 2004, "Clinical Accuracy Evaluation of Femoral Canal Preparation Using the Robodoc System," J. Orthop. Sci., **9**(5), pp. 452–461.

[8] Honl, M., Dierk, O., Gauck, C., Carrero, V., Lampe, F., Dries, S., Quante, M., Schwieger, K., Hille, E., and Morlock, M. M., 2003, "Comparison of Robotic-Assisted and Manual Implantation of a Primary Total Hip Replacement: A Prospective Study," J. Bone Joint Surg., **85**(8), pp. 1470–1478.

[9] Hackney, M. E., and Earhart, G. M., 2009, "Effects of Dance on Movement Control in Parkinson's Disease: A Comparison of Argentine Tango and American Ball-Room," J. Rehabil. Med., **41**(6), pp. 475–481.

[10] Knapp, M. L., Hall, J. A., and Horgan, T. G., 2013, *Nonverbal Communication in Human Interaction*, Cengage Learning, Wadsworth, Boston, MA.

[11] Feth, D., Groten, R., Peer, A., Hirche, S., and Buss, M., 2009, "Performance Related Energy Exchange in Haptic Human-Human Interaction in a Shared Virtual Object Manipulation Task," World Haptics 2009-Third Joint EuroHaptics Conference and Symposium on Haptic Interfaces for Virtual Environment and Teleoperator Systems, Salt Lake City, UT, Mar. 18–20, IEEE, New York, pp. 338–343.

[12] Stefanov, N., Peer, A., and Buss, M., 2009, "Role Determination in Human-Human Interaction," World Haptics 2009-Third Joint EuroHaptics Conference and Symposium on Haptic Interfaces for Virtual Environment and Teleoperator Systems, Salt Lake City, UT, Mar. 18–20, IEEE, New York, pp. 51–56.

[13] Reed, K. B., and Peshkin, M. A., 2008, "Physical Collaboration of Human-Human and Human-Robot Teams," IEEE Trans. Haptic, **1**(2), pp. 108–120.

[14] Sylos-Labini, F., d'Avella, A., Lacquaniti, F., and Ivanenko, Y., 2018, "Human-Human Interaction Forces and Inter-Limb Coordination During Side-by-Side Walking With Hand Contact," Front. Physiol., **9**, p. 179.
[15] Hogan, N., 1987, "Stable Execution of Contact Tasks Using Impedance Control," Proceedings of the 1987 IEEE International Conference on Robotics and Automation, Raleigh, NC, Mar. 31–Apr. 3, Vol. 4, IEEE, New York, pp. 1047–1054.
[16] Sawers, A., Bhattacharjee, T., McKay, J. L., Hackney, M. E., Kemp, C. C., and Ting, L. H., 2017, "Small Forces That Differ with Prior Motor Experience can Communicate Movement Goals During Human-Human Physical Interaction," J. Neuroeng. Rehabil., **14**(1), p. 8.
[17] van der Linde, R. Q., and Lammertse, P., 2003, "Hapticmaster–A Generic Force Controlled Robot for Human Interaction," Ind. Rob., **30**(6), pp. 515–524.
[18] Massie, T. H., and Salisbury, J. K., 1994, "The Phantom Haptic Interface: A Device for Probing Virtual Objects," Proceedings of the ASME Winter Annual Meeting, Symposium on Haptic Interfaces for Virtual Environment and Teleoperator Systems, Chicago, IL, Nov. 6–11, Vol. 55, Citeseer, pp. 295–300.
[19] Salisbury, J. K., and Srinivasan, M. A., 1997, "Phantom-Based Haptic Interaction with Virtual Objects," IEEE Comput. Graphics Appl., **17**(5), pp. 6–10.
[20] Scott, S. H., 1999, "Apparatus for Measuring and Perturbing Shoulder and Elbow Joint Positions and Torques During Reaching," J. Neurosci. Methods, **89**(2), pp. 119–127.
[21] Hogan, N., Krebs, H. I., Charnnarong, J., Srikrishna, P., and Sharon, A., 1993, "Mit-Manus: A Workstation for Manual Therapy and Training," SPIE Application in Optical Science and Engineering, Boston, MA, Mar. 26, Vol. 1833, Telemanipulator Technology, pp. 28–34.
[22] Chen, T. L., Bhattacharjee, T., McKay, J. L., Borinski, J. E., Hackney, M. E., Ting, L. H., and Kemp, C. C., 2015, "Evaluation by Expert Dancers of a Robot That Performs Partnered Stepping via Haptic Interaction," PLoS One, **10**(5), p. e0125179.
[23] Wang, Z., Yuan, J., and Buss, M., 2008, "Modelling of Human Haptic Skill: A Framework and Preliminary Results," Proceedings of the 17th IFAC World Congress, Seoul, South Korea, July 6–11, pp. 14761–14766.
[24] Schaal, S., Sternad, D., Osu, R., and Kawato, M., 2004, "Rhythmic Arm Movement Is Not Discrete," Nat. Neurosci., **7**(10), pp. 1136–1143.
[25] Pandilov, Z., and Dukovski, V., 2014, "Comparison of the Characteristics Between Serial and Parallel Robots," Acta Tech. Corvininesis-Bull. Eng., **7**(1), pp. 143–160.
[26] Patel, Y. D., and George, P. M., 2012, "Parallel Manipulators Applications—A Survey," Mod. Mech. Eng., **2**(3), pp. 57–64.
[27] Campos, L., Bourbonnais, F., Bonev, I. A., and Bigras, P., 2010, "Development of a Five-Bar Parallel Robot With Large Workspace," Proceeding of the ASME 2010 IDETC/CIE, Montreal, QC, Canada, Aug. 15–18, Citeseer, pp. 917–922.
[28] Alıcı, G., 2000, "Determination of Singularity Contours for Five-Bar Planar Parallel Manipulators," Robotica, **18**(5), pp. 569–575.
[29] Asada, H., and Youcef-Toumi, K., 1984, "Analysis and Design of a Direct-Drive Arm with a Five-Bar-Link Parallel Drive Mechanism," ASME J. Dyn. Syst. Meas. Contr., **106**(3), pp. 225–230.
[30] Chablat, D., and Wenger, P., 1999, "Regions of Feasible Point-to-Point Trajectories in the Cartesian Workspace of Fully-Parallel Manipulators," hal-00145125, pp. 1–6.
[31] Bonev, I., and Gosselin, C. M., 2001, "Singularity Loci of Planar Parallel Manipulators with Revolute Joints," Proceedings of the 2nd Workshop on Computational Kinematics, Seoul, Korea, May 20–22, Vol. 41, pp. 219–299.
[32] Basu, P. S., and Farhang, K., 1994, "Kinematic Analysis and Design of Two-Input, Five-Bar Mechanisms Driven by Relatively Small Cranks," ASME J. Mech. Des., **116**(4), pp. 1108–1114.
[33] Midha, A., Cipra, R., and Farhang, K., 1985, "Analysis and Design of Basic Linkages for Harmonic Motion Generation," ASME J. Mech., Trans., Automation, **107**(4), pp. 499–506.
[34] Song, Y. S., and Hogan, N., 2015, "A Novel Interactive Exoskeletal Robot for Overground Locomotion Studies in Rats," IEEE Trans. Neural Syst. Rehabil. Eng., **23**(4), pp. 591–599.
[35] Midha, A., and Zhao, Z.-L., 1985, "Synthesis of Planar Linkage via Loop Closure and Nonlinear Equations Solution," Mech. Mach. Theory, **20**(6), pp. 491–502.
[36] yu Chao, W., yuan Xin, H., Wei, W., and jia Rong, L., 2017, "Frictional Analysis of Deep-Groove Ball Bearings with Varying Circumference Radial Preloads," Adv. Mech. Eng., **9**(5), p. 1687814017703895.
[37] Armstrong, B., 1988, "Friction: Experimental Determination, Modeling and Compensation," Proceedings of the 1988 IEEE International Conference on Robotics and Automation, Philadelphia, PA, Apr. 24–29, Vol. 3, IEEE, New York, pp. 1422–1427.
[38] Quach, N., and Liu, M., 2000, "Friction Torque Estimation and Compensation for Robot Arms," Proceedings of the Australia, Conference on Robotics and Automation, Melbourne, Australia, Aug. 30–Sept. 1, Citeseer, pp. 211–216.
[39] Flash, T., and Mussa-Ivaldi, F., 1990, "Human Arm Stiffness Characteristics During the Maintenance of Posture," Exp. Brain Res., **82**(2), pp. 315–326.